Journal of Solid State Chemistry 297 (2021) 122047

Contents lists available at ScienceDirect

Journal of Solid State Chemistry

journal homepage: www.elsevier.com/locate/jssc

Effect of Sm-doping on microstructure and thermoelectric properties of textured *n*-type $Bi_2Te_{2.7}Se_{0.3}$ compound due to change in ionic bonding fraction

Maxim Yaprintsev [a], Oleg Ivanov [a,b,*], Alexei Vasil'ev [a], Marina Zhezhu [a], Ekaterina Yaprintseva [a]

[a] Belgorod State University, Belgorod, 394015, Federation, Russia
[b] Belgorod State Technological University Named After V.G. Shukhov, Belgorod, 308012, Federation, Russia

ARTICLE INFO

Keywords:
Doping effect
Bismuth telluride
Thermoelectric properties
Ionic bonding fraction
Grain structure
Texturing

ABSTRACT

Textured *n*-type $Bi_{2-x}Sm_xTe_{2.7}Se_{0.3}$ compounds with $x = 0$; 0.005; 0.02 and 0.05 have been prepared by microwave-solvothermal synthesis of starting powders and spark plasma sintering of bulk materials. Texturing [001] axis coincided with direction of spark plasma sintering pressuring. With increasing x, (i) an average lateral size of grains in the samples is decreasing; (ii) the Lotgering factor characterizing a degree of preferential orientation of the grains is increasing; (iii) anomalies of all the thermoelectric properties, related to onset of intrinsic conductivity, are shifted to higher temperatures. The Sm-doping effect on the grain structure and thermoelectric properties of samples is attributed to increasing in ionic bonding fraction, which can occur at increasing Sm content due to a difference in electronegativity of Bi and Sm atoms. Maxima in temperature dependences of the thermoelectric figure-of-merit, typical for Bi_2Te_3-based compounds and due to the intrinsic conductivity, were observed. The highest value of the thermoelectric figure-of-merit was found to be weakly dependent on x and falling into ~0.6 ÷ ~0.7 interval, whereas temperature position of the maxima is remarkably shifted to higher temperatures with increasing Sm content.

1. Introduction

Elemental doping is known to be fruitful and effective way to improve thermoelectric performance of materials [1–3]. Particularly, rare earth elements, R (R = Lu, Tm, Ce, Gd etc.), can be used as promising dopants to remarkably enhance the thermoelectric figure-of-merit, ZT, of low-temperature thermoelectric materials, based on bismuth telluride, Bi_2Te_3 [4–15]. ZT is given as $ZT = [PF/k_t]T$, where T is the absolute temperature, k_t is the total thermal conductivity and PF is the power factor [16]. In turn, PF is expressed as $PF = S^2/\rho$, where ρ is the specific electrical resistivity and S is the Seebeck coefficient. Main mechanisms of R-doping effect on ZT are as follows: (i) an increase of electron concentration, since rare earth elements behave as donors in crystal lattice of Bi_2Te_3; b) an increase of electron and phonon scattering by various point defects, which are forming in the lattice under doping; c) a formation of narrow non-parabolic impurity band with a high density of states near the Fermi level that affect both the Seebeck coefficient and the thermal conductivity. Besides, one more, at least, mechanism should be also involved to account for varying in the thermoelectric properties of the grained Bi_2Te_3 and Bi_2Te_3-based compounds, doped with rare earth elements. This mechanism is related to a possible change of chemical bonding in the Bi_2Te_3 structure. The crystal Bi_2Te_3 structure is layered one [17–19]. Crystal c-axis is oriented perpendicularly to the layers, and the neighboring layers are bonded via weak Van-der-Waals interaction. Crystal (a–b)-planes are oriented along the layers, and the chemical bonding between atoms within the layers is dominantly strong covalent with small fraction of ionic bonding. For R-doped material, an ionic boding fraction, *I.F.*, can be changed, since the electronegativity of Bi (X_{Bi}) and R (X_R) atoms are rather different. The change should be dependent on $\Delta X_{Bi\text{-}R} = X_{Bi} - X_R$ (or type of R atom), and R-doping level (or content of R-dopant). In turn, varying between the covalent and ionic contributions into the chemical bonding of the R-doped Bi_2Te_3-doped compounds can affect their physical and chemical properties, and processes, which are related to these properties. Particularly, a growth of Bi_2Te_3 particles during chemical synthesis can be partially governed by features of the chemical bonding in the particles being growing. If a starting powder consisting of these particles will be next applied to prepare relevant grained bulk material, features of grain structure

* Corresponding author. Belgorod State Technological University named after V.G. Shukhov, Belgorod, 308012, Federation, Russia.
E-mail address: Ivanov.Oleg@bsu.edu.ru (O. Ivanov).

https://doi.org/10.1016/j.jssc.2021.122047
Received 19 November 2020; Received in revised form 28 January 2021; Accepted 2 February 2021
Available online 6 February 2021

formation in this material will be strongly dependent on shape and size of the particles in the starting powder. In turn, the features of the grain structure can remarkably affect the thermoelectric properties of the Bi_2Te_3-based materials [20–24].

The aim of present work is to find and analyze the Sm-doping effect on the grain structure and thermoelectric properties of the textured *n*-type $Bi_2Te_{2.7}Se_{0.3}$ compound.

2. Materials and methods

Microwave-solvothermal synthesis and spark plasma sintering (SPS) methods were applied to prepare the $Bi_{2-x}Sm_xTe_{2.7}Se_{0.3}$ compounds with $x = 0$; 0.005; 0.02 and 0.05. To synthesize the starting powders, analytically pure chemicals ($Bi(NO_3)_3{\cdot}5H_2O$, TeO_2, SeO_2, $Sm(NO_3)_3{\cdot}6H_2O$, NaOH, poly(1-ethenylpyrrolidin-2-one), ethane-1,2-diol) were used. At the first synthesis stage, $Bi(NO_3)_3{\cdot}5H_2O$, TeO_2, $Sm(NO_3)_3{\cdot}6H_2O$, taken in a stoichiometric ratio in accordance with x, were dissolved in mixture of 90 cm^3 ethane-1,2-diol NaOH and 15 g NaOH under vigorous stirring by a magnetic stirrer. Poly(1-ethenylpyrrolidin-2-one) (Mr = 12 000) was then added to the reaction mixture and this mixture was again under vigorous stirring for 30 min. After, the autoclave was sealed and maintained at 190°C for 5 min, and then cooled to room temperature naturally. As soon as the reaction was completed, dark grey precipitate was taken out by centrifuging and washed with deionized water and ethyl alcohol several times and then dried at 80°C for 8 h. To prepare the bulk samples, the starting powders were twice spark-plasma-sintered. Each of the SPS-process was implemented at pressure of 40 MPa and temperature of 680 K for 2 min in vacuum. To study the thermoelectric properties, the 2 × 2 × 10 mm bars and the Ø10 × 1 mm disks were prepared.

Density of the bulk samples was measured by the Archimedes' method. Transmission electron JEM - 2100 microscope was applied to characterize the starting powder. X-ray diffraction (XRD) analysis was performed by a Rigaku Ultima IV diffractometer with CuK_α - radiation to identify crystal structure and phase composition of the starting powders and the bulk samples. Scanning electron microscopy (SEM) using a Nova NanoSEM 450 microscope was applied to observe starting powder morphology, estimate average particles size and study grain structure features of the bulk samples. Energy dispersive X-ray spectroscopy (EDX) method was applied to map distributions of chemical elements for the particles in the starting powder and on the surface of the bulk samples. The Bi-L, Sm-L, Te-L and Se–K characteristic lines were used to plot the maps. Spectra of the particles and surface were recorded by an Oxford Instruments INCA Energy dispersive spectrometer (JEM-2100 microscope) and EDAX Octane Elect EDS System energy dispersive spectrometer (Nova NanoSEM 450 microscope), respectively. The EDX method applied is characterized by an energy resolution of 120 eV and a concentration resolution up to 0.1%.

To determine correct elemental composition of the bulk samples, a Shimadzu ICP (Inductively Coupled Plasma) emission spectrometer ICPE-9000 was applied. The specific electrical resistivity and Seebeck coefficient of the bar samples were measured by using a ZEM-3 system. The total thermal conductivity of the disk-shaped samples was measured by a TC-1200 system using a laser flash method.

3. Results and discussion

3.1. Effect of the Sm-doping on synthesis of the starting powders

According to XRD analysis, the starting $Bi_{2-x}Sm_xTe_{2.7}Se_{0.3}$ powders with different x are single rhombohedral $R\bar{3}m$ phase, which is characteristic of pure Bi_2Te_3 (PDF#01-089-4302). For instance, XRD pattern for the starting powder with $x = 0.05$ is shown in Fig. 1. Difference between the ionic radii of Bi and Sm is small enough [25]. Therefore, the Sm-doping effect on the lattice parameters of Bi_2Te_3 would be too small

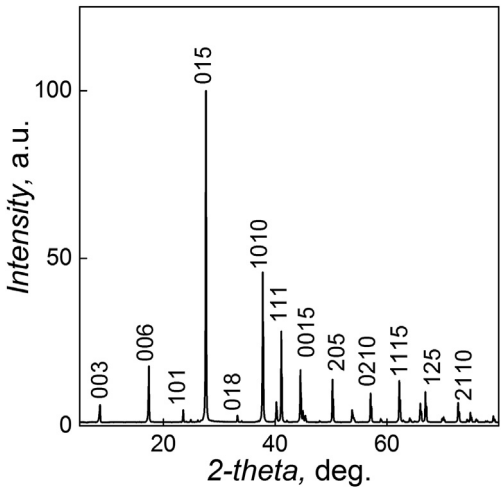

Fig. 1. XRD pattern for the starting $Bi_{1.95}Sm_{0.05}Te_{2.7}Se_{0.3}$ powder.

to found in XRD patterns, taken for compositions with different x. As result, the lattice parameters, $a = b$ and c, are x-independent and equal to 4.354 and 30.355 Å, respectively.

According to SEM examination, the starting powders mainly consisted of hexagonal plate-shaped particles. For instance, SEM image for the starting powder with $x = 0.05$ is shown in Fig. 2. Forming the plate-shaped particles during the chemical synthesis is typical for the Bi_2Te_3-based compounds and can be attributed to specific features of the crystal structure and chemical bonding of Bi_2Te_3 [17–19].

According to EDX mapping of the Bi, Te, Sm and Se distributions, taken for individual particles of the starting powders, all the elements are uniformly distributed within the particles. For instance, the maps for the starting powder with $x = 0.05$ are shown in Fig. 3. According to results of selected area electron diffraction (SAED), taken for individual $Bi_{1.95}Sm_{0.05}Te_{2.7}Se_{0.3}$ particle (Fig. 3 (e)), the particle is single-crystalline with the crystal Bi_2Te_3 structure (Fig. 3 (f)).

It is important to note that the sizes of the plate-shaped particles are dependent on Sm content. To estimate the average lateral size, D_a, and the average thickness, d_a, of the particles, histograms of the lateral size and thickness distributions were plotted for the starting powders with different x. The average D_a and d_a sizes were next extracted by analyzing the histograms in frames of a lognormal unimodal distribution [26]. At increasing Sm content, D_a is gradually decreasing from ~525 nm for $x = 0$ down to ~425 nm for $x = 0.05$, whereas d_a retains to be unchanged and equal to ~50 nm for all the compositions (Fig. 4). To clear these features, mechanisms of the Bi_2Te_3 particles growth, which is implemented during the solvothermal synthesis of the starting powder, should be considered in detail [27–31]. Bi_2Te_3 has rhombohedral structure corresponding to the tetradymite type. As was mentioned above, this structure is usually

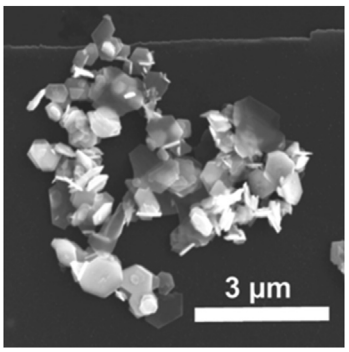

Fig. 2. SEM image for the starting $Bi_{1.95}Sm_{0.05}Te_{2.7}Se_{0.3}$ powder.

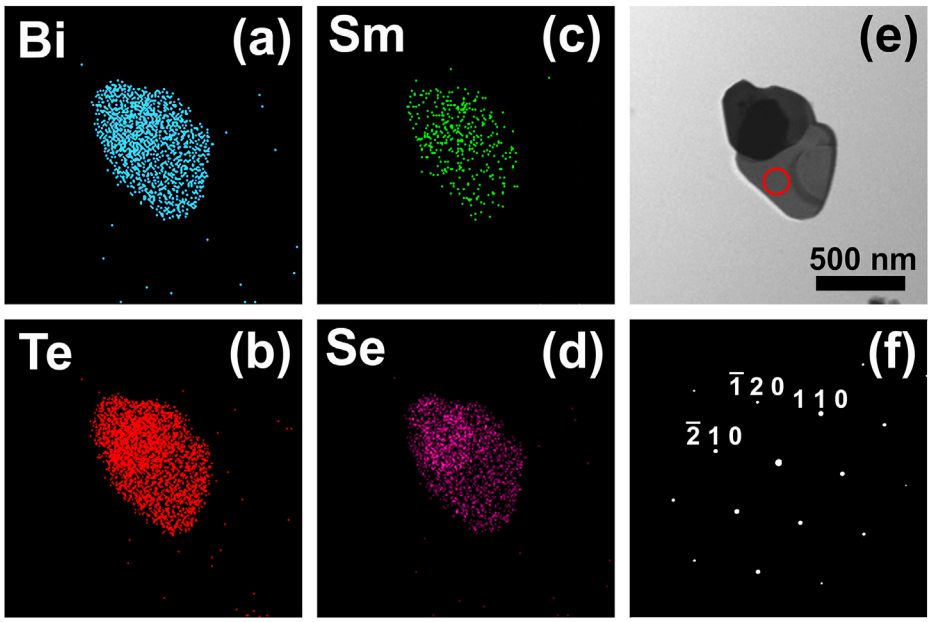

Fig. 3. Maps of the Bi (a), Te (b), Sm (c) and Se (d) distributions, taken within several individual $Bi_{1.95}Sm_{0.05}Te_{2.7}Se_{0.3}$ particles, which are shown in TEM image (e), and SAED pattern (f), taken for one of these particles.

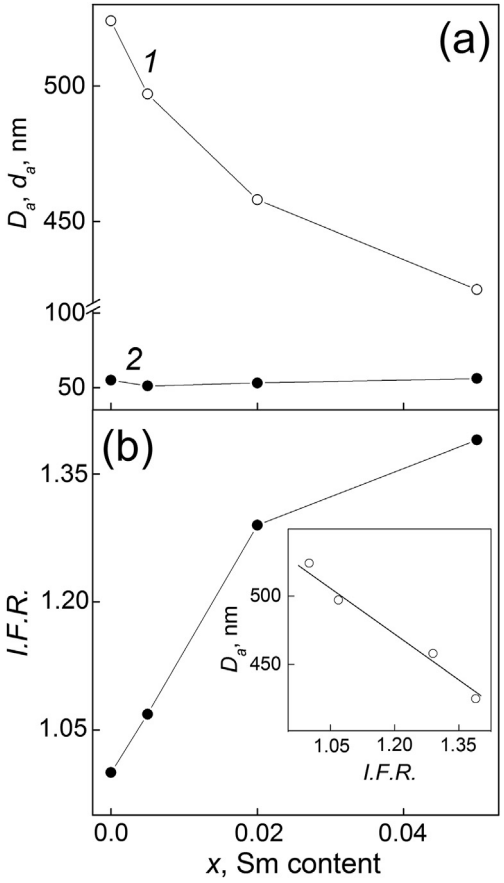

Fig. 4. Effect of the Sm-doping on the average lateral size (D_a, curve *1*) and the average thickness (d_a, *2*) of the particles in the starting powders (a), and on the ionic fraction (*I.F.R.*) ratio (b). Inset: the D_a vs. *I.F.R.* dependence.

described in terms of the layered structure, and the layers are positioned perpendicularly to *c* - axis. The five individual atomic layers are stacked in the following order

Te(1)–Bi–Te(2)–Bi–Te(1), (1)

Where Te(1) and Te(2) denote two types of Te in the lattice.

Bismuth atoms are octahedrally coordinated by tellurium atoms, and the Te(2) atoms are octahedrally coordinated by Bi. The Te(1) atoms are covalently bonded with three Bi atoms on one side and by weaker Van-der-Waals bonds with three other Te(1) atoms on the other side. The Bi–Te(1) bond length is close to the expected covalent bond length, while the Bi–Te(2) bond rather corresponds to the value expected for ionic bonding [32,33].

There are several mechanisms of the Bi_2Te_3 particles growth during the solvothermal synthesis. The basic process, which is implementing during the synthesis, is based on "monoatom model" [31]. According to this model, individual atoms or ions are combined to a nucleus growing in a solution and then other atoms or ions attach to the nucleus leading to the particle growth. If single Te atom or Te^{2-} ion from the solution attaches itself to the Te(1)-layered crystal surface, then they will probably jump back into the solution, since the Van-der-Waals bonding is not strong enough to fix the atom on the surface, which coincides with base (*a*–*b*)-plane in the crystal Bi_2Te_3 structure. However, an interaction between atoms via polar-covalent bonding, which corresponds to the interlayered Bi–Te(1) or Bi–Te(2) interaction, is strong enough to fix the atom on the lateral surface of the Bi_2Te_3 nucleus. As result, the lateral growth of the Bi_2Te_3 particles is remarkably accelerating. Therefore, the particle will grow faster in (*a*–*b*)- plane than in direction of *c*–axis, resulting in the plate-shaped particles as shown in Fig. 2.

Since the ionic bonding partially exists in the Bi_2Te_3 particles, these particles can possess the properties of ionic crystals. It is known that during synthesis of ionic crystals from polar solutions, the processes of growth and dissolution are simultaneously competing [34–36]. The rate of growth and shape of the crystal being growing are originated from a result of this competition. Ionic crystals can be characterized by the ionic boding fraction (*I.F.*). In accordance with the empirical Pauling expression, *I.F.* is related to a difference in the electronegativity of interacting *A* and *B* atoms (ions) as follows [37].

$$I.F. = 1 - \left[exp\left\{ -\frac{(\Delta X)^2}{4} \right\} \right] \times 100\ \%, \quad (2)$$

where X_A and X_B are the electronegativities of atoms (ions), and $\Delta X = X_A - X_B$.

By a partial substituting *A* or/and *B* ions for other *C* ion (*C*-doping), *I.F.* can be increased (at X_A-$X_C > X_A$-X_B or X_C-$X_B > X_A$-X_B that will results in increasing ΔX) or decreased (at X_A-$X_C < X_A$-X_B or X_C-$X_B < X_A$-X_B that will results in decreasing ΔX). For the $Bi_{2-x}Sm_xTe_{2.7}Se_{0.3}$ compounds, the electronegativities of elements are $X_{Bi} = 2.02$, $X_{Sm} = 1.17$, $X_{Te} = 2.10$ and $X_{Se} = 2.55$. Since X_{Sm}-$X_{Bi} > X_{Te}$-X_{Bi}, *I.F.* should be gradually increasing with increasing Sm content [38]. To roughly estimate changing in *I.F.*, which is due to the Sm-doping, expression (2) can be applied. Difference in the Te(1)-Bi and Te(2)-Bi bonding will be neglected. Besides, since only partial substitution of Sm for Bi takes place, the $X_{Bi\text{-}Sm} = [(1\text{-}x)\cdot X_{Bi} + x\cdot X_{Sm}]$ expression will be introduced to take into account changing in the X_{Bi} and X_{Sm} contributions into the total electronegativity of the Sm-doped compounds with different *x*. To take into account the different electronegativities of Te and Se, the $X_{Te\text{-}Se} = [0.9\cdot X_{Te} + 0.1\cdot X_{Se}]$ expression was also used. Then, ΔX was calculated as $\Delta X = X_{Bi\text{-}Sm}$–$X_{Te\text{-}Se}$. The calculated *I.F.* values are too small, although relative change of *I.F.*, which is originated from the Sm-doping, is remarkably enough. To show this change, *I.F.* was recalculated to an ionic fraction ratio, $I.F.R. = I.F.(x)/I.F.(x = 0)$. The *I.F.R.* vs. Sm content dependence is shown in Fig. 4 (b).

I.F.R is expectedly growing with increasing *x*, and the maximum *I.F.R.* value is equal to ~1.4. It is important to note that the average lateral size of the $Bi_{2-x}Sm_xTe_{2.7}Se_{0.3}$ particles is linearly decreasing, when *I.F.R.* is gradually increasing (inset to Fig. 4 (b)). This trend can be attributed to change of a dissolution process that acts during the synthesis of the particles of ionic crystal from a polar solution. The solution, applied to solvothermally synthesize the $Bi_{2-x}Sm_x$ $Te_{2.7}Se_{0.3}$ particles, is polar one. The dissolution process is based on the electrostatic interaction between ions containing in the particles being growing, and polar molecules containing in the solution [36]. Increasing in the ionic boding fraction can enhance this interaction, and the dissolution process will become more effective. As results, the average lateral size of the particles will be decreasing with increasing *I.F.R.* that is, in turn, governed by increasing in Sm content. The growth of the $Bi_{2-x}Sm_x$ $Te_{2.7}Se_{0.3}$ particles along the perpendicular direction (along *c*-axis) is based on the weak Van-der-Waals interaction. This interaction is *x* (or *I.F.R*)-independent. Therefore, the thickness of the particles is *x* (or *I.F.R.*)–independent, too.

3.2. Effect of the Sm-doping on the grain structure of the bulk samples

The starting $Bi_{2-x}Sm_x$ $Te_{2.7}Se_{0.3}$ powders with different *x* were next spark-plasma-sintered to prepare the bulk samples. The density of the bulk samples is very weakly *x*-dependent and equal to 7.5 g/cm^3 that is ~96% of the theoretical density for $Bi_2Te_{2.7}Se_{0.3}$ (7.78 g/cm^3, according to Ref. [10]). According to ICP analysis, elemental composition of all the bulk samples is in well agreement with their nominal composition (Table 1).

To confirm homogeneous contributions of the chemical elements in the bulk samples, EDX maps of the Bi, Te, Se and Sm distributions were plotted for the polished surfaces of the $Bi_{2-x}Sm_xTe_{2.7}Se_{0.3}$ samples with different *x*. Really, all the elements including Sm were homogeneously distributed per the surfaces. The maps for the sample with $x = 0.05$ are shown in Fig. 5. All the bulk samples are highly textured. Texturing (001)

Table 1
Elemental composition of the bulk $Bi_{2-x}Sm_xTe_{2.7}Se_{0.3}$ samples with different *x*.

Sample	Element (at. %)			
	Bi	Sm	Te	Se
$Bi_2Te_{2.7}Se_{0.3}$	39.95	–	54.11	5.94
$Bi_{1.995}Sm_{0.005}Te_{2.7}Se_{0.3}$	40.06	0.08	53.85	6.01
$Bi_{1.98}Sm_{0.02}Te_{2.7}Se_{0.3}$	39.55	0.42	54.12	5.91
$Bi_{1.95}Sm_{0.05}Te_{2.7}Se_{0.3}$	38.96	0.99	53.97	6.08

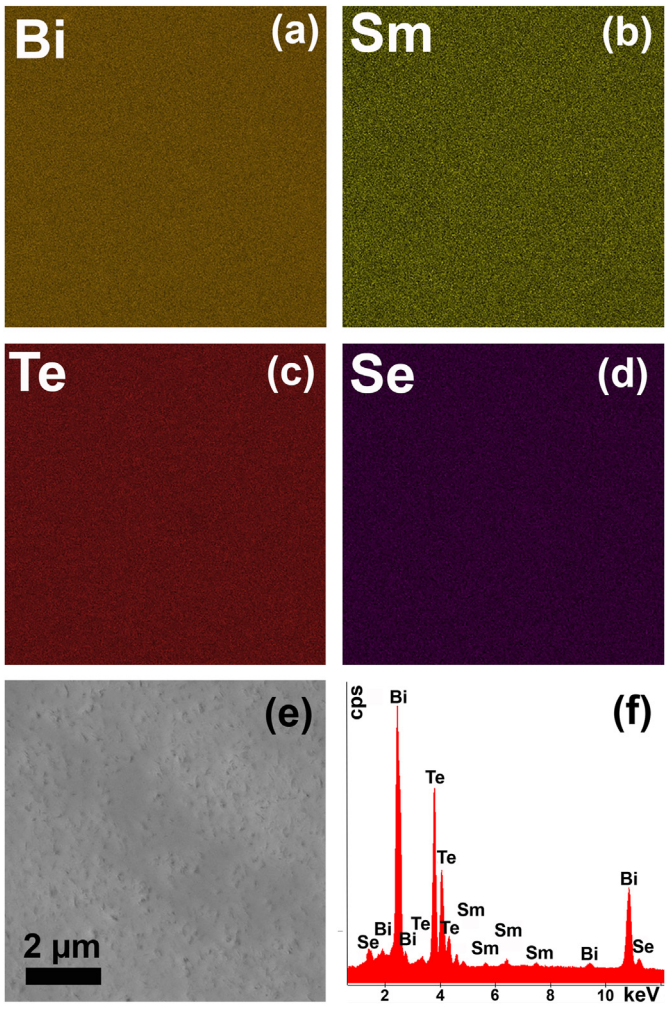

Fig. 5. Maps of the Bi (a), Sm (b), Te (c) and Se (d) distributions for the bulk $Bi_{1.95}Sm_{0.05}Te_{2.7}Se_{0.3}$ sample; SEM image of the polished surface applied to plot the maps (e); the EDX spectrum of the surface.

axis coincides with SPS-pressuring direction. Features in the texturing of the Bi_2Te_3-based materials have been reported in detail in Ref. [39]. Generally, the texturing can be directly observed in SEM images of the grain structures, recorded on fractured surfaces oriented parallel and perpendicularly to SPS-pressing direction. These SEM images taken for the bulk $Bi_{1.95}Sm_{0.05}Te_{2.7}Se_{0.3}$ sample are presented in Fig. 6.

Disordered grain structure with the grains having mainly irregular shape is observed at the fractured surface, which is perpendicular to SPS-pressing direction (Fig. 6 (a)), whereas at the fractured surface, which is parallel to this direction, the grains form ordered lamellar structure (Fig. 6 (b)). The lamellar sheets consist of the grains, which are elongated in plane oriented perpendicularly to SPS-pressing direction. As result, the average grain sizes, measured in directions parallel ($D_\perp$) and perpendicular ($D_\parallel$) to SPS-pressing direction, are different. To estimate the average grain size in both directions, histograms of the grain size distributions were plotted for the bulk samples with different *x*. The lognormal unimodal distribution was again applied to analyze the histograms. The $D_\perp$ and $D_\parallel$ dependences were next extracted (Fig. 7).

Similarly to the Sm-doping effect on the D_a and d_a sizes for the particles in the starting powders, it was found that at increasing Sm content, $D_\perp$ is gradually decreasing from ~800 nm for $x = 0$ down to ~665 nm for $x = 0.05$, whereas $D_\parallel$ is slightly increasing from ~110 nm for $x = 0$ up to ~115 nm for $x = 0.05$. In other words, increasing Sm content results in decreasing in the lateral grain size in the lamellar sheets, but change of the grain thickness is very weak. For all the compositions, $D_\perp/D_a$ and $D_\parallel/$

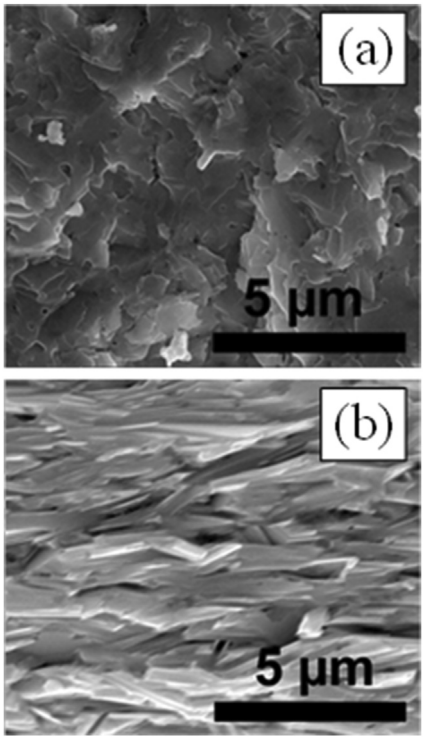

Fig. 6. SEM images taken on the fractured surfaces, oriented perpendicular (a) and parallel (b) to SPS-pressing direction for the bulk $Bi_{1.95}Sm_{0.05}Te_{2.7}Se_{0.3}$ sample.

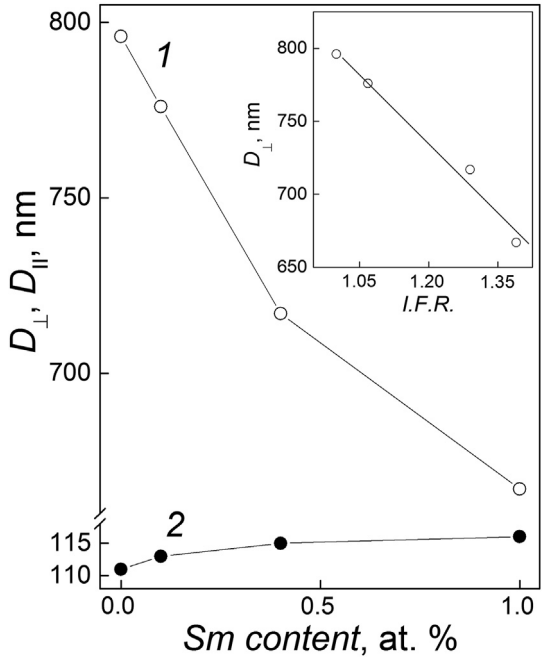

Fig. 7. Effect of the Sm-doping on the average grain sizes, measured in directions perpendicular ($D_\perp$, curve *1*) and parallel ($D_\parallel$, *2*) to SPS-pressing direction (a); Inset: the $D_\perp$ vs. *I.F.R.* dependence.

d_a ratios, which characterize the lateral growth and thickness growth of the grains, respectively, are equal to ~1.55 and ~2.2. Thus, the final $D_\perp$ and $D_\parallel$ sizes of the grains in the bulk samples are dominantly governed by the initial D_a and d_a sizes of the particles in the relevant starting powder.

The texturing in the Bi_2Te_3-based compounds is also accompanied by redistribution of intensity for some peaks in XRD patterns taken from surfaces, oriented parallel and perpendicularly to the texturing axis. For the parallel surface, the 00*l* peaks are dominant, whereas all other peaks are strongly weakened. For the surface perpendicular to this direction, the 11*l* peaks are already dominant. A texturing degree, which characterizes a degree of preferential grains orientation, is usually estimated by the Lotgering factor [40], *F*. The *F* value for the bulk samples with different *x* was estimated by analysis of XRD patterns presented in Fig. 8 by using expressions

$$F = \frac{p - p_0}{1 - p_0}, \tag{3a}$$

with p and p_0 are defined as

$$p = \frac{I(00l)}{\sum I(hkl)}, \text{ and } p_0 = \frac{I_0(00l)}{\sum I_0(hkl)} \tag{3b}$$

where the intensities I and I_0 correspond to textured and non-textured samples, respectively. In limiting cases, $F \to 1$ is for ideally textured (like single crystal) samples, and $F \to 0$ is for completely non-textured samples (powder or grained material with completely random grain orientation). XRD patterns taken for the starting powders were used to analyze the intensities in XRD pattern for the non-textured samples.

The Lotgering factor is gradually increased with increasing Sm content. This trend is clearly confirmed by growth of the 006 peak intensity, which occurs with increasing *x* (Fig. 8). The *F* versus Sm content dependence is shown in Fig. 9. Inset to Fig. 9 shows the *F* versus *I.F.R.* dependence. The Sm-doping effect on *F* observed is very strong and unexpected. It should be noted that increasing in the ionic bonding fraction, originated from increasing Sm content, is accompanied by decreasing in the lateral size of the starting powder particles (inset to Fig. 4 (a)). It is known [41] that the initial stage of the SPS process is a packing of the particles of the starting powder under external pressure. In this case, the grain growth can be ignored and densification of the powder being sintered is dominantly related to the particles rotation and sliding. The rotation and sliding processes for two plate-shaped particles with equal size *d* are schematically shown in Fig. 10.

The particle I is oriented perpendicularly to SPS pressuring direction (*P*). In the initial state (at time t_0), the particles are disoriented to each

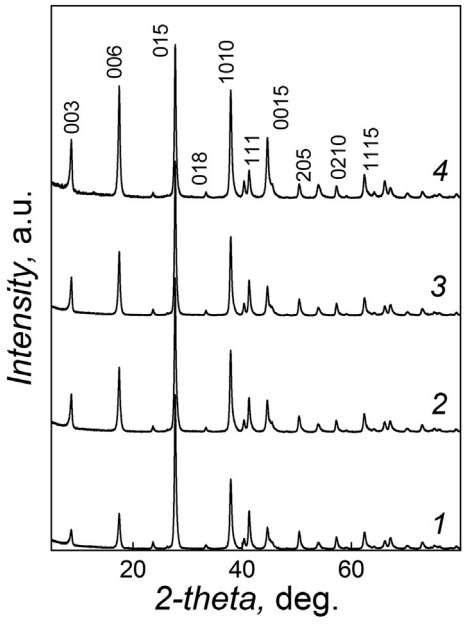

Fig. 8. XRD patterns for the bulk $Bi_{2-x}Sm_xTe_{2.7}Se_{0.3}$ samples with $x = 0$ (curve *1*); 0.005 (*2*); 0.02 (*3*) and 0.05 (*4*), taken from the surfaces oriented parallel to the texturing axis.

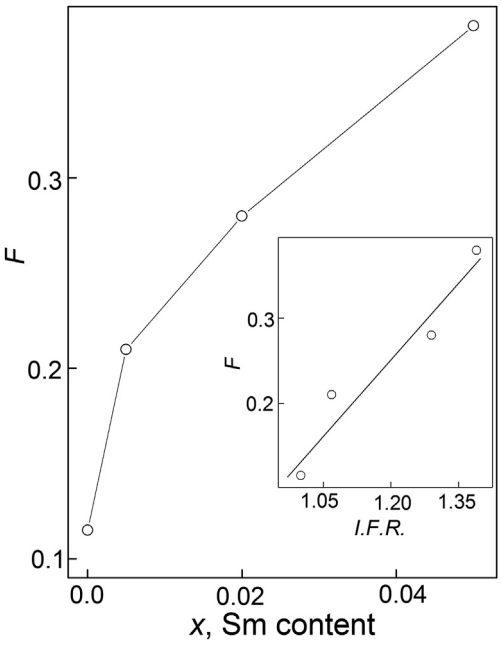

Fig. 9. Effect of the Sm-doping on the Lotgering factor (*F*). Inset: the *F* vs. *I.F.R.* dependence.

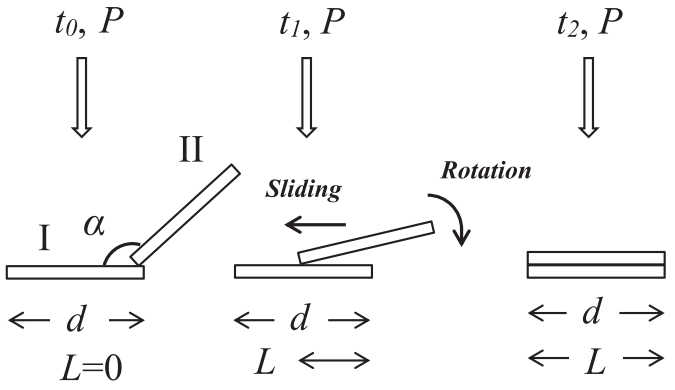

Fig. 10. Schematic of rearrangement of the particles under the packing of the starting powder during the SPS process.

other. The disorientation angle is α. During the SPS process, the particle II starts to rotate and slide along the surface of the particle I, as is shown for time t_1. Friction force will be preventing the sliding. The sliding distance is *L*. At ideal texturing, two particles should be finally rearranged parallel to each other, resulting in forming of the lamellar grain structure (at time t_2). Obviously, *L* will be dependent on *d*. During forming the lamellar grain structure, the fine particles will be rearranging more readily as compared to that for the coarse particles. So, the preferential grains orientation will be increasing with decreasing *d*.

3.3. Effect of the Sm-doping on the thermoelectric properties

The thermoelectric properties of the textured Bi_2Te_3-based compounds, measured parallel or perpendicularly to the texturing axis, are quite different [39,42–46]. Better properties, allowing maximizing the thermoelectric figure-of-merit, correspond to the perpendicular measuring direction. Hence, only these properties are analyzed here. The temperature dependences of ρ, *S* and *PW*, taken for the samples with different *x*, are shown in Fig. 11 (a), (b), (c) and (d), respectively. The $\rho(T)$ and $S(T)$ dependences are typical for the Bi_2Te_3 and Bi_2Te_3-based

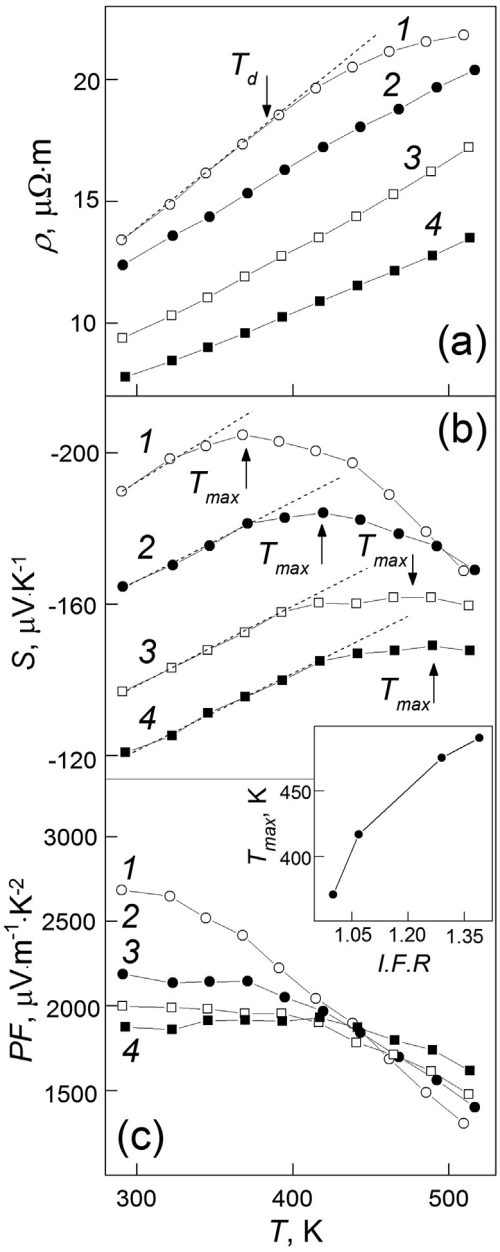

Fig. 11. The ρ (a), *S* (b) and *PF* (c) vs. *T* dependences for the $Bi_{2-x}Sm_xTe_{2.7}Se_{0.3}$ samples with $x = 0$ (curves *1*); 0.005 (*2*); 0.02 (*3*) and 0.05 (*4*). Inset: the T_m vs. *I.F.R.* dependence.

compounds [4–15,39,46]. Main features in these dependences are related to onset of the intrinsic conductivity at high temperature, which is due to a thermal excitation of carriers from valence band to conduction band. The intrinsic conductivity is accompanied by appearance of kinks in the $\rho(T)$ dependences at temperature T_d (Fig. 11 (a)) and maxima in the $S(T)$ dependences at temperature T_{max} (Fig. 11 (b). These anomalies are indicated by arrows in Figures. To not complicate Fig. 11 (a), the arrow is shown only in the $\rho(T)$ dependence for the sample with $x = 0$.

The electrical resistivity of solids, in which electrons are the majority carriers, is expressed as $\rho = 1/(en\mu)$, where *e* is the charge of electron, and *n* and μ are the concentration and the mobility of electrons, respectively. The $\rho(T)$ dependence, taken below the ρ kink, corresponds to regime of degenerate semiconductor. In this case, the electron concentration is *T*-independent, and the $\rho(T)$ behavior is mainly governed by temperature behavior of the electron mobility. Above the ρ kink, the thermal generation of electrons and holes, which is due to the intrinsic conductivity,

takes place, that, in turn, results in increase of the carriers concentration and relevant decrease of ρ. The kink in the $\rho(T)$ dependence just reflects this gradual change in the conductivity mechanism.

Sign of the Seebeck coefficient is negative that is in agreement with electron conductivity of the samples being studied. All the $S(T)$ curves in Fig. 11 (b) are bell-like shaped that is also related to a bipolar effect. It is known [47] that the Seebeck coefficient of degenerate semiconductor can be expressed as

$$S = \frac{2k_B^2 T m^*}{3e\hbar^2}\left(\frac{\pi}{3n}\right)^{2/3}\left(\frac{3}{2}+\gamma\right), \quad (4)$$

where k_B is the Boltzmann's constant, $\hbar$ is the reduced Planck constant, m^* is the density-of-state effective mass of electrons and γ is the scattering factor.

Below the S maxima, all the $S(T)$ dependences are T-linear, that is in agreement with expression (4). Above the S maxima, which are positioned at T_{max}, the bipolar effect becomes dominant one. To implement the bipolar effect, electrons and holes should be simultaneously presented in solid. The thermal excitation of carries due to the intrinsic conductivity does not change the majority carriers concentration too much, whereas the minority carriers concentration will be remarkably increasing. The S sign for the electron conductivity is negative, and it is positive for the hole conductivity. Competing of two S contributions having opposite signs is resulted in forming of the $S(T)$ maxima. Both the electrical resistivity and the Seebeck coefficient are steady falling with increasing x. These trends can be reasonably related to increasing in the electron concentration under the Sm-doping. The temperature dependences of the power factor are presented in Fig. 11 (c). These dependences account for the ρ and S contributions. At low temperatures (before onset of the intrinsic conductivity), PW is steady decreasing with increasing the Sm content, but at high temperatures, PW is already changed in the opposite manner.

The ρ and S anomalies, observed at T_d and T_{max}, respectively, are shifted to higher temperatures with increasing Sm content. This trend is the most pronounced in shifting of the $S(T)$ maximum (inset to Fig. 11). In general, to induce the intrinsic conductivity, the thermal energy of carries should be high enough to they can overcome a band gap, E_g. In turn, the thermal energy is proportional to absolute temperature. Then, shifting of the $S(T)$ maximum to higher temperatures can be resulted from relevant increasing in E_g under the Sm-doping. It is important to note that covalent crystals usually are semiconductors, whereas ionic crystals belong to insulators [48]. Partial increasing in the ionic bonding fraction, which should be resulted from the Sm-doping, could increase E_g and shifts relevant anomalies of the thermoelectric properties, which are due to the intrinsic conductivity, to higher temperatures. It would be useful to estimate E_g for the samples with different x. Generally, the $S(T)$ dependences can be applied to estimate the band gap as the bipolar conductivity takes place. Really, in accordance with the Goldsmid-Sharp expression [49], the band gap, the maximum value of the Seebeck coefficient ($|S|_{max}$.) and the temperature at which it occurs (T_{max}), are related as $E_g = 2e|S|_{max}T_{max}$. By using the experimental data ($|S|_{max} \approx$ 210 μV/K and $T_m \approx$ 375 K for undoped Bi_2Te_3), the Goldsmid-Sharp expression results in the E_g estimate equal to ~0.16 eV. This estimate is remarkably less then value of ~0.21 eV known for $Bi_2Te_{2.7}Se_{0.3}$ [10]. To account this difference, a validity of the Goldsmid-Sharp expression for the $Bi_2Te_{2.7}Se_{0.3}$ compound should be analyzed. According to Ref. [50], the Goldsmid-Sharp expression is invalid when either the majority-to-minority weighted mobility ratio is very different from 1.0 or as E_g becomes significantly smaller than $10k_BT$. For narrow-gaped semiconductors ($E_g \leq 6\ k_BT$), the Maxwell-Boltzmann statistic, which results in the Goldsmid-Sharp expression, breaks down and the Fermi-Dirac statistic is already required. A product of $6k_BT_m$ is equal to ~0.19 eV. Thus, the $Bi_2Te_{2.7}Se_{0.3}$ sample behaves as narrow-gaped semiconductor for which the Goldsmith-Sharp expression cannot be correctly applied to estimate E_g.

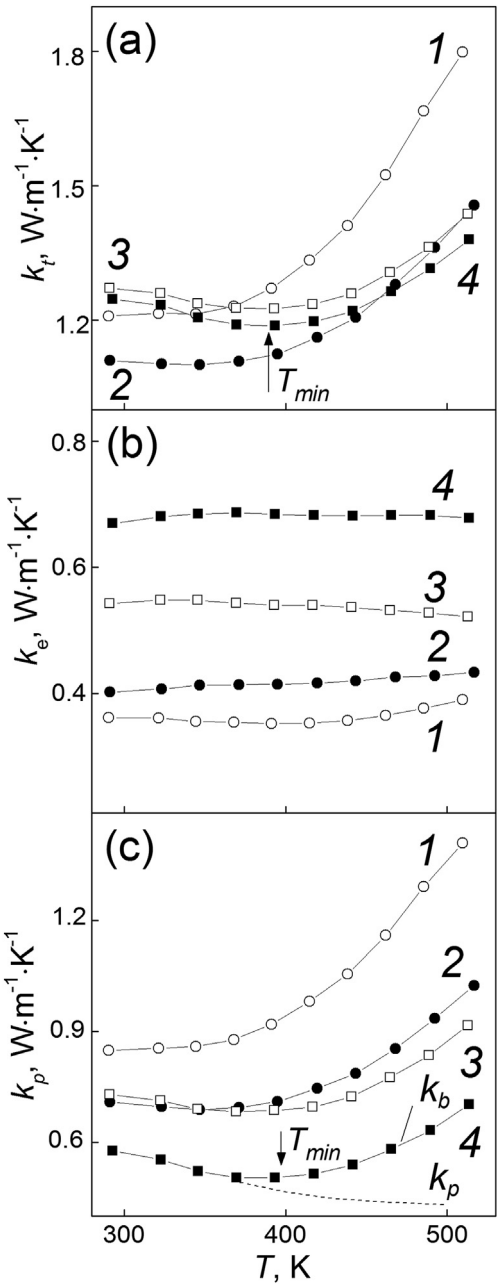

Fig. 12. The k_t (a), k_e (b) and k_p (c) vs. T dependences for the $Bi_{2-x}Sm_xTe_{2.7}Se_{0.3}$ samples with $x = 0$ (curves *1*); 0.005 (*2*); 0.02 (*3*) and 0.05 (*4*).

The temperature dependences of k_t are presented in Fig. 12 (a). All the $k_t(T)$ dependences has minima at temperature T_{min} (T_{min} is x-dependent), which are originated from change in the thermal conductivity mechanism. This minimum is indicated by arrow for the sample with $x = 0.05$. The $k_t(T)$ behavior is combined from contributions from the electron thermal conductivity k_e, the lattice thermal conductivity, k_p, and the bipolar thermal conductivity, k_b. The k_e contribution is related to the specific electrical conductivity, $\sigma = 1/\rho$, through the Wiedemann-Franz law

$$k_e = L\sigma T, \quad (5)$$

where L is the Lorenz number.

Approach proposed in Ref. [51] was further applied to estimate the Lorenz number for the samples being studied. According to this approach, a relation between L and the maximum value of the Seebeck coefficient can be expressed as

$$L\left[10^{-8},\ \mathrm{W}\cdot\Omega\cdot\mathrm{K}^{-2}\right] = 1.5 + \exp\left(-\frac{|S|_{max}\left[\mu\mathrm{V}\cdot\mathrm{K}^{-1}\right]}{116}\right), \quad (6)$$

By using expression (6) and experimental data (Fig. 10 (b)), the Lorenz number was estimated for all the samples. These L values was used to extract the $k_e(T)$ contributions, as is shown in Fig. 12 (b). Since ρ is decreasing with increasing x, k_e is changed in opposite manner. The lattice thermal conductivity contributions were extracted as $k_p(T) = k_t(T) - k_e(T)$ (Fig. 12 (c)). Similarly to the $k_t(T)$ dependences, all the $k_p(T)$ curves have minima at ($T_{\min}$ is also x-dependent).

Below $T_{\min}$, the $k_p(T)$ contributions are gradually decreasing with increasing temperature. Really, above the Debye temperature, k_p is usually varied as T^{-1}, as is shown be dashed line for the sample with $x = 0.05$ [47]. In accordance with the Dulong-Petit law, for these temperatures the phonon specific heat is a constant and phonon energy (and number of phonons) increases linearly with increasing temperature. The lattice thermal conductivity is gradually decreasing with increasing Sm content. Therefore, the Sm atoms can act as the scattering center for phonons resulting in depressing of k_p. The k_p growth above $T_{\min}$ is originated from a bipolar thermal conductivity [52]. Due to the intrinsic conductivity, electron-hole pairs are thermally excited at the hot-side of the sample. These pairs start moving to the cold-side, where they are recombined. The energy of recombination per one pair is naturally equal or greater than the band gap. This energy is emerged as a phonon, which transfers a heat. This process is main mechanism of k_b. The $k_b(T)$ dependences are shifted to higher temperatures with increasing Sm content that is agreement with the $S(T)$ behavior (Fig. 11 (b)). This trend can be also related to increase of the band gap, which, in turn, is attributed to increase of the ionic bonding fraction under the Sm-doping.

Finally, the $PW(T)$ and $k_t(T)$ dependences were used to calculate the ZT dependences for the samples with different x (Fig. 13). All the ZT dependences have maxima at temperature T_M. The ZT maxima are originated from the intrinsic conductivity developing at high temperatures and resulting in falling S (Fig. 11 (b)) and growing k_t (Fig. 12 (a)). The highest ZT value is weakly x-dependent and falling into the ~0.6 ÷ ~0.7 interval. The Sm-doping results in reducing both the specific electrical resistivity and the lattice thermal conductivity that is favoring to enhancing in the thermoelectric figure-of-merit. Unfortunately, at the same time the Seebeck coefficient decreases and the electron thermal conductivity increases that result in reducing in the thermoelectric figure-of-merit. As result of two competing trends in the Sm-doping effect on the thermoelectric properties, the thermoelectric figure-of-merit of the $Bi_{2-x}Sm_xTe_{2.7}Se_{0.3}$ compounds is weakly sensitive to the Sm dopant.

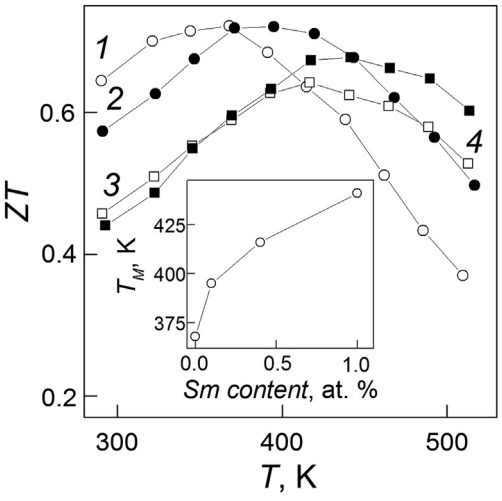

Fig. 13. The ZT vs. T dependences for the $Bi_{2-x}Sm_xTe_{2.7}Se_{0.3}$ samples with $x =$ 0 (curves *1*); 0.005 (*2*); 0.02 (*3*) and 0.05 (*4*). Inset: the $T_{\max}$ vs. Sm content dependence.

Thus, the Sm-doping did not allow enhancing the thermoelectric figure-of-merit of $Bi_{2-x}Sm_xTe_{2.7}Se_{0.3}$ for the x range studied. However, T_M is remarkably shifted to higher temperatures with increasing x (inset to Fig. 13). This feature may be important for thermoelectric applications, since it could change an operating temperatures interval of thermoelectric devices.

4. Conclusion

To analyze the Sm-doping effect of the grain structure and the thermoelectric properties of the textured *n*-type $Bi_{2-x}Sm_xTe_{2.7}Se_{0.3}$ compounds, possible changing in the ionic bonding fraction has been taken into account. This change is due to difference in the electronegativity of the Bi and Sm atoms. Main features of x-dependent changes in the grain structure and thermoelectric properties of the compounds could be attributed to varying in the ionic bonding fraction under doping.

CRediT authorship contribution statement

Maxim Yaprintsev: Project administration. **Oleg Ivanov:** Conceptualization, Writing - review & editing. **Alexei Vasil'ev:** Investigation. **Marina Zhezhu:** Investigation. **Ekaterina Yaprintseva:** Investigation.

Declaration of competing interest

The authors declare that they have no known competing financial interests or personal relationships that could have appeared to influence the work reported in this paper.

Acknowledgments

This work was supported by the Russian Foundation for Basic Research (grant number No 20-03-00672). All of studies were carried out by the scientific equipment of joint research center "Technologies and Materials" at the Belgorod State University.

References

[1] Y. Pan, T.R. Wei, C.F. Wu, J.F. Li, Electrical and thermal transport properties of spark plasma sintered *n*-type $Bi_2Te_{3-x}Se_x$ alloys: the combined effect of point defect and Se content, J. Mater. Chem. C. 3 (2015) 10583–10589. https://doi.org/10.1039/C5TC02219C.

[2] L. Hu, T. Zhu, X. Liu, X. Zhao, Point defect engineering of high-performance bismuth-telluride-based thermoelectric materials, Adv. Funct. Mater. 24 (2014) 5211–5218. https://doi:10.1002/adfm.201400474.

[3] J. Suh, K.M. Yu, D. Fu, X. Liu, F. Yang, J. Fan, D.J. Smith, Y.H. Zhang, J.K. Furdyna, C. Dames, W. Walukiewicz, J. Wu, Simultaneous enhancement of electrical conductivity and thermopower of Bi_2Te_3 by multifunctionality of native defects, Adv. Mater. 27 (2015) 3681–3686. https://doi:10.1002/adma.201501350.

[4] M. Yapryntsev, A. Vasil'ev, O. Ivanov, Sintering temperature effect on thermoelectric properties and microstructure of the grained $Bi_{1.9}Gd_{0.1}Te_3$ compound, J. Eur. Ceram. Soc. 39 (2019) 1193–1205, https://doi.org/10.1016/j.jeurceramsoc.2018.12.041.

[5] J. Yang, F. Wu, Z. Zhu, L. Yao, H. Song, X. Hu, Thermoelectrical properties of lutetium-doped Bi_2Te_3 bulk samples prepared from flower-like nanopowders, J. Alloys Compd. 619 (2015) 401–405. https://doi:10.1016/j.jallcom.2014.09.024.

[6] X.H. Ji, X.B. Zhao, Y.H. Zhang, B.H. Lu, H. Ni, Synthesis and properties of rare earth containing Bi_2Te_3 based thermoelectric alloys, J. Alloys Compd. 387 (2005) 282–286. https://doi.org/10.1016/j.jallcom.2004.06.047.

[7] F. Wu, H. Song, J. Jia, X. Hu, Effects of Ce, Y, and Sm doping on the thermoelectric properties of Bi_2Te_3 alloy, Prog. Nat. Sci. Mater. Int. 23 (2013) 408–412. https://doi:10.1016/j.pnsc.2013.06.007.

[8] F. Wu, W. Shi, X. Hu, Preparation and thermoelectric properties of flower-like nanoparticles of Ce-Doped Bi_2Te_3, Electron, Mater. Lett. 11 (2015) 127–132. https://doi:10.1007/s13391-014-4139-x.

[9] X.H. Ji, X.B. Zhao, Y.H. Zhang, B.H. Lu, H.L. Ni, Solvothermal synthesis and thermoelectric properties of lanthanum contained Bi–Te and Bi–Se–Te alloys, Mater. Lett. 59 (2005) 682–685. https://doi:10.1016/j.matlet.2004.11.008.

[10] F. Wu, H.Z. Song, J.F. Jia, F. Gao, Y.J. Zhang, X. Hu, Thermoelectric properties of Ce-doped *n*-type $Ce_xBi_{2-x}Te_{2.7}Se_{0.3}$ nanocomposites, Phys. Status Solidi 210 (2013) 1183–1189. https://doi:10.1002/pssa.201228589.

[11] W.Y. Shi, F. Wu, K.L. Wang, J.J. Yang, H.Z. Song, X.J. Hu, Preparation and thermoelectric properties of yttrium-doped Bi_2Te_3 flower-like nanopowders,

J. Electron. Mater. 43 (2014) 3162–3168. https://doi:10.1007/s11664-014-3220-4.
[12] X.B. Zhao, Y.H. Zhang, X.H. Ji, Solvothermal synthesis of nano-sized $La_xBi_{(2-x)}Te_3$ thermoelectric powders, Inorg. Chem. Commun. 7 (2004) 386–388. https://doi:10.1016/j.inoche.2003.12.020.
[13] O. Ivanov, M. Yaprintsev, R. Lyubushkin, O. Soklakova, Enhancement of thermoelectric efficiency in Bi_2Te_3 via rare earth element doping, Scripta Mater. 146 (2018) 91–94. https://doi:10.1016/j.scriptamat.2017.11.031.
[14] M. Yaprintsev, R. Lyubushkin, O. Soklakova, O. Ivanov, Effects of Lu and Tm doping on thermoelectric properties of Bi_2Te_3, J. Electron. Mater. 47 (2018) 1362–1370. https://doi:10.1007/s11664-017-5940-8.
[15] O. Ivanov, M. Yaprintsev, Mechanisms of thermoelectric efficiency enhancement in Lu-doped Bi_2Te_3, Mater. Res. Express 5 (2018), 015905-1-10, https://doi:10.1088/2053-1591/aaa265.
[16] G.J. Snyder, Figure of merit ZT of a thermoelectric device defined from materials properties, Energy Environ. Sci. 10 (2017) 2280–2283. https://doi:10.1039/c7ee02007d.
[17] H.J. Goldsmid, Bismuth telluride and its alloys as materials for thermoelectric generation, Mater 7 (2014) 2577–2592. https://doi:10.3390/ma7042577.
[18] H. Scherrer, S. Scherrer, Thermoelectrics Handbook: Macro to Nano, CRC Taylor and Francis, Boca Raton, 2012.
[19] G.S. Nolas, J. Sharp, H.J. Goldsmid, Thermoelectrics Basic Principles and New Materials Developments, Springer, Berlin, 2001.
[20] M.G. Kanatzidis, Nanostructured thermoelectrics: the new paradigm, Chem. Mater. 22 (2009) 648–659. https://doi:10.1021/cm902195j.
[21] O. Ivanov, O. Maradudina, R. Lyubushkin, Grain size effect on electrical resistivity of bulk nanograined Bi_2Te_3 material, Mater. Char. 99 (2015) 175–179. https://doi:10.1016/j.matchar.2014.12.001.
[22] M. Takashiri, K. Miyazaki, S. Tanaka, J. Kurosaki, D. Nagai, H. Tsukamoto, Effect of grain size on thermoelectric properties of *n*-type nanocrystalline bismuth-telluride based thin films, J. Appl. Phys. 104 (2008), 084302 -1-6, https://doi:10.1063/1.2990774.
[23] O. Ivanov, M. Yaprintsev, A. Vasil, ev, Anisotropy of the grain size effect on the electrical resistivity of *n*-type $Bi_{1.9}Gd_{0.1}Te_3$ thermoelectric textured by spark plasma sintering, J. Eur. Ceram. Soc. 40 (2020) 3431–3436. https://doi:10.1016/j.jeurceramsoc.2020.03.048.
[24] S. Yoon, O.-J. Kwon, S. Ahn, J.-Y. Kim, H. Koo, S.-H. Bae, J.-Y. Cho, J.-S. Kim, C. Park, The effect of grain size and density on the thermoelectric properties of Bi_2Te_3-PbTe compounds, J. Electron. Mater. 42 (2013) 3390–3396. https://doi:10.1007/s11664-013-2753-2.
[25] Y.Q. Jia, Crystal radii and effective ionic radii of the rare earth ionsJ, Sol. State. Chem. 95 (1991) 184–187. https://doi:10.1016/0022-4596(91)90388-X.
[26] F.J. Humphreys, M. Hatherly, Recrystallization and Related Annealing Phenomena, Elsevier, Oxford, UK, 2004.
[27] T. Ludwig, L. Guo, P. McCrary, Z. Zhang, H. Gordon, H. Quan, M. Stanton, R.M. Frazier, R.D. Rogers, H.-T. Wang, C.H. Turner, Mechanism of bismuth telluride exfoliation in an ionic liquid solvent, Langmuir 31 (2015) 3644–3652. https://doi:10.1021/acs.langmuir.5b00239.
[28] B. Hamawandi, S. Ballikaya, H. Batili, V. Roosmark, M. Orlovská, A. Yusuf, M. Johnsson, R. Szukiewicz, M. Kuchowicz, M.S. Toprak, Facile solution synthesis, processing and characterization of *n*- and *p*-type binary and ternary Bi–Sb tellurides, Appl. Sci. 10 (2020), 1178-1-13, https://doi:10.3390/app10031178.
[29] D. Li, X.Y. Qin, Y.F. Liu, N.N. Wang, C.J. Song, R.R. Sun, Improved thermoelectric properties for solution grown $Bi_2Te_{3-x}Sex$ nanoplatelet composites, RSC Adv. 3 (2013) 2632–2638. https://doi:10.1039/c2ra22562j.
[30] M. Loor, G. Bendt, U. Hagemann, C. Wölper, W. Assenmacher, S. Schulz, Synthesis of Bi_2Te_3 and $(Bi_xSb_{1-x})_2Te_3$ nanoparticles using the novel IL $[C4mim]_3[Bi_3I_{12}]$, Dalton Trans. 45 (2016) 15326–15335. https://doi:10.1039/c6dt02361d.
[31] X.B. Zhao, X.H. Ji, Y.H. Zhang, G.S. Cao, J.P. Tu, Hydrothermal synthesis and microstructure investigation of nanostructured bismuth telluride powder, Appl. Phys. A 80 (2005) 1567–1571. https://doi:10.1007/s00339-004-2956-8.
[32] J.R. Drabble, C.H.L. Goodman, Chemical bonding in bismuth telluride, J. Phys. Chem. Solid. 5 (1958) 142–144. https://doi:10.1016/0022-3697(58)90139-2.
[33] S. Nakajima, The crystal structure of $Bi_2Te_{3-x}Se_x$, J. Phys. Chem. Solid. 24 (1963) 479–485. https://doi:10.1016/0022-3697(63)90207-5.
[34] M.N. Joswiak, M.F. Doherty, B. Peters, Ion dissolution mechanism and kinetics at kink sites on NaCl surfaces, Proc. Natl. Acad. Sci. Unit. States Am. 115 (2018) 656–661. https://doi:10.1073/pnas.1713452115.
[35] L.J. Wang, J.W. Lu, F.S. Xu, F.S. Zhang, Dynamics of crystallization and dissolution of calcium orthophosphates at the near-molecular level, Chin. Sci. Bull. 56 (2011) 713–721. https://doi:10.1007/s11434-010-4184-2.
[36] M. Kowacz, M. Prieto, A. Putnis, Kinetics of crystal nucleation in ionic solutions: electrostatics and hydration forces, Geochem. Cosmochim. Acta 74 (2010) 469–481. https://doi:10.1016/j.gca.2009.10.028.
[37] R.T. Sanderson, Electronegativity and bond energy, J. Am. Chem. Soc. 105 (1983) 2259–2261. https://doi:10.1021/ja00346a026.
[38] G.D. Sproul, Evaluation of electronegativity scales, ACS Omega 5 (2020) 11585–11594, https://doi.org/10.1021/acsomega.0c00831.
[39] O. Ivanov, M. Yaprintsev, A. Vasil'ev, Comparative analysis of the thermoelectric properties of the non-textured and textured $Bi_{1.9}Gd_{0.1}Te_3$ compounds, J. Solid State Chem. 290 (2020), 121559-1-10, https://doi:10.1016/j.jssc.2020.121559.
[40] F.K. Lotgering, Topotactical reactions with ferrimagnetic oxides having hexagonal crystal structures—I, J. Inorg. Nucl. Chem. 9 (1959) 113–123. https://doi:10.1016/0022-1902(59)80070-1.
[41] L. Wang, V. Pouchly, K. Maca, Z. Shen, Y. Xiong, Intensive particle rearrangement in the early stage of spark plasma sintering process, J. Asian Ceram. Soc. 3 (2015) 183–187. https://doi:10.1016/j.jascer.2015.02.004.
[42] S.D. Bhame, D. Pravarthana, W. Prellier, J.G. Noudem, Enhanced thermoelectric performance in spark plasma textured bulk *n*-type Bi2Te2.7Se0.3 and p-type Bi0.5Sb1.5Te3, Appl. Phys. Lett. 102 (2013), 2190-2191-3, http://doi:10.1063/1.4807771.
[43] J. Jiang, L. Chen, S. Bai, Q. Yao, Q. Wang, Fabrication and thermoelectric performance of textured *n*-type $Bi_2(Te,Se)_3$ by spark plasma sintering, Mater. Sci. Eng. B 117 (2005) 334–338. https://doi:10.1016/j.mseb.2005.01.002.
[44] Q. Lognon, F. Gascoin, O.I. Lebedev, L. Lutterotti, S. Gascoin, D. Chateigner, Quantitative texture analysis of spark plasma textured *n*-Bi_2Te_3, J. Am. Ceram. Soc. 97 (2014) 2038–2045. https://doi:10.1111/jace.12970.
[45] J.J. Shen, L.P. Hu, T.J. Zhu, X.B. Zhao, The texture related anisotropy of thermoelectric properties in bismuth telluride based polycrystalline alloys, Appl. Phys. Lett. 99 (2011), 124102-1-3, https://doi:10.1063/1.3643051.
[46] M. Yaprintsev, A. Vasil'ev, O. Ivanov, Thermoelectric properties of the textured $Bi_{1.9}Gd_{0.1}Te_3$ compounds spark-plasma-sintered at various temperatures, J. Eur. Ceram. Soc. 40 (2020) 742–750. https://doi:10.1016/j.jeurceramsoc.2018.12.041.
[4][7] K.C. Lukas, W.C. Liu, Z.F. Ren, C.P. Opeil, Transport properties of Ni, Co, Fe, Mn doped $Cu_{0.01}Bi_2Te_{2.7}Se_{0.3}$ for thermoelectric device applications, J. Appl. Phys. 112 (2012), 054509-1-5, https://doi:10.1063/1.4749806.
[48] J.S. Blakemore, Solid State Physics, Cambridge University Press, Cambridge, 1985.
[49] H.J. Goldsmid, J.W. Sharp, Estimation of the thermal band gap of a semiconductor from Seebeck measurements, J. Electron. Mater. 28 (1999) 869–872. https://doi:10.1007/s11664-999-0211-y.
[50] Z.M. Gibbs, H.-S. Kim, H. Wang, G.J. Snyder, Band gap estimation from temperature dependent Seebeck measurement – deviations from the $2e|S|_{max}T_{max}$ relation, Appl. Phys. Lett. 106 (2015), 022112-1-5, https://doi:10.1063/1.4905922.
[51] H. Kim, Z. Gibbs, Y. Tang, H. Wang, G. Snyder, Characterization of Lorenz number with Seebeck coefficient measurement, Apl. Mater. 3 (2015), 041506-1-5, https://doi:10.1063/1.4908244.
[52] S. Wang, J. Yang, T. Toll, J. Yang, W. Zhang, X. Tang, Conductivity-limiting bipolar thermal conductivity in semiconductors, Sci. Rep. 5 (2015), 10136-1-5, https://doi:10.1038/srep10136.